The influence of crystallite size on the structural stability of Cu/SAPO-34 catalysts

Siyuan Huang[a], Jun Wang[a], Jianqiang Wang[a], Chen Wang[a], Meiqing Shen[a,b,c,*], Wei Li[d,**]

[a] *Key Laboratory for Green Chemical Technology of State Education Ministry, School of Chemical Engineering & Technology, Tianjin University, Tianjin 300072, PR China*
[b] *State Key Laboratory of Engines, Tianjin University, Tianjin 300072, PR China*
[c] *Collaborative Innovation Center of Chemical Science and Engineering, Tianjin 300072, PR China*
[d] *General Motors Global Research and Development, Chemical Sciences and Materials System Lab, 30500 Mound Road, Warren, MI 48090, USA*

ARTICLE INFO

ABSTRACT

A series of Cu/SAPO-34 catalysts of identical chemical compositions but different crystallite sizes (1–13 μm) was prepared by "one-pot" method. The fresh and low-temperature hydrothermally treated (LHT) catalysts were characterized by a comprehensive set of techniques, including XRF, SEM, EDS, XRD, NMR, BET, XPS, pyridine-FTIR, NH$_3$ and diethylamine TPD, EPR as well as H$_2$-TPR. The reaction rates for NH$_3$-SCR were measured under differential conditions and correlated with their physical and chemical properties. All fresh catalysts, regardless of crystallite size, showed the same bulk properties, such as chemical composition, crystallinity, acidity and copper species. After a hydrothermal treatment (96 h at 70 °C with 80% humidity), loss of micropore surface area, micro volume, relative crystallinities, acidity and isolated Cu^{2+} species was observed on all catalysts, and the extent of decrease was proportional to the average crystallite size. NH$_3$-SCR reaction rate suffered a similar decrease with increasing crystallite size. Surface analyses by SEM-ESD, XPS and diethylamine-TPD showed an obvious surface enrichment of Si (and Brønsted acidity) on all fresh catalysts, and the degree of enrichment is also proportional to crystallite size. This surface enrichment of Si-O-Al linkages is thought to be the root cause for the structural vulnerability found on larger crystallite catalysts under LHT conditions. This understanding is entirely consistent with the observation found on the H/SAPO-34 reference materials of the same sizes, where the structural destruction is even more severe after the LHT. A mechanism for structural disintegration for larger Cu/SAPO-34 crystals was proposed, and the genesis of the Si gradient was discussed in the context of crystallization kinetics.

1. Introduction

Copper-exchanged small-pore molecular sieves with a Chabazite structure (Cu/CHA), e.g., Cu/SSZ-13 and Cu/SAPO-34, were reported to be excellent catalysts for the selective reduction of NO$_x$ using NH$_3$ (NH$_3$-SCR). Because of their high SCR activity and N$_2$ selectivity in a broad temperature window, they are the most studied catalytic materials for NO$_x$ emission control from diesel vehicles [1–4]. For vehicle applications, catalyst hydrothermal stability is a key requirement. In that regard, Cu-SSZ-13 and Cu/SAPO-34 face different kinds of challenges in catalyst stability [5,6]. Cu/SSZ-13 was found to deactivate after a high-temperature hydrothermal aging treatment, presumably as a result of aggregation of isolated Cu^{2+} ions into CuO$_x$ clusters and even dealumination [7]. Cu/SAPO-34, on the other hand, behaves quite

differently; although it has a good high-temperature hydrothermal ability, it suffers poor low-temperature hydrothermal durability [8–11].

In early studies, silicoaluminophosphates (SAPO-n) materials were reported to show poor structural stability when they were exposed to a relative humidity above 40% at room temperature. For SAPO-34, an irreversible loss of crystallinity was discovered upon low-temperature hydration, and this structure degradation was thought to be caused by the Si-O-Al bonds breakage [12]. It was reported that the low-temperature stability of SAPO-34 was also related to the structural directing template used for the material synthesis [13,14]. For example, samples synthesized using morpholine as a template showed a lower stability than those using TEAOH. This could be rationalized by the large quantity of the Si-O-Al bonds in the materials made using morpholine, which are more prone to attach by water. Mees et al. [15] proposed that

---

replacing protons on the Brønsted acid sites by NH_4^+ species could prevent structural deterioration. Recently, Leistner and Olsson [10] reported that the NH_3-SCR activity of Cu/SAPO-34 catalysts decreased significantly after exposing the catalysts in H_2O containing feed at 70 °C for several hours. Cao et al. [16] reported that the NH_3-SCR activity loss after hydration treatment at 80 °C is revealed to be caused by the decrease of acid sites (Si-O-Al bonds) and the variation of reducibility of Cu^{2+} ions. Previously, we reported that the low-temperature hydrothermal ability of Cu/SAPO-34 could be improved by increasing the copper loading or the number of isolated Cu^{2+} ions on the catalyst [17]. The isolated Cu^{2+} ions on the exchangeable sites of SAPO-34 can stabilize the framework structure by preventing H_2O to attack the Si-O-Al bonds.

Although the intrinsic activity and activation energy for fresh Cu/SAPO-34 catalysts were shown to be independent of crystallite size for NH_3-SCR reaction [18], the role of crystallite size on low-temperature hydrothermal stability was not clear. However, there are some indications in literature that crystallite size of SAPO-34 catalyst might be important for their durability. In the study of MTO reaction, some literatures reported that it took a much shorter time to completely deactivate the large-crystal SAPO-34 catalyst compared with the small-crystal SAPO-34 catalyst [19,20].

The objective of this study is to understand how crystallite size of the Cu-SAPO-34 catalyst influences its low-temperature hydrothermal stability. According to literature, the prevailing mechanism for Cu/SAPO-34 deactivation is via Si-O-Al bonds breakage. Thus, we were particularly interested in determining the elemental distribution (especially for Si) within a crystal as a function of crystallite size. Through a systematic study of a series of fresh and low-temperature hydrothermally aged Cu/SAPO-34 and H/SAPO-34 samples of different crystallite sizes but identical chemical composition, using NH_3-SCR reaction and a variety of characterization techniques, we are able to establish a quantitative relationship between crystallite size and surface elemental composition and therefore between crystallite size and structural stability. The origin of different concentration gradients of elements within Cu/SAPO-34 crystals is also discussed in relation to the kinetics of crystallization.

2. Experimental

2.1. Sample preparation

A series of Cu/SAPO-34 catalysts was synthesized using a modified one-pot method, which was described by Prakash et al. [21] and others [22–25]. The synthesis gel had a molar composition of 1 Al_2O_3 : 1 P_2O_5 : 0.5 SiO_2 : 0.1 CuO : 2 morpholine (MOR) : 0.05 tetraethylenepentamine (TEPA) : 61.7 H_2O. The sources of Si, P, Al and Cu were silica sol (40 wt% SiO_2, Qingdao Jiyida Silica Reagent Factory), orthophosphoric acid (85 wt% H_3PO_4, Tianjin Kemiou Chemical Reagent Co., Ltd.), pseudoboehmite (68 wt% Al_2O_3, Shandong Aluminium Industry Co., Ltd.), and copper (II) sulfate pentahydrate (Purity above 99 wt%, Tianjin Guangfu Chemical Reagent Co., Ltd.). MOR (Purity above 99 wt%, Tianjin Kemiou Chemical Reagent Co., Ltd.) was used as a template agent and TEPA (Purity above 99 wt%, Tianjin Kemiou Chemical Reagent Co., Ltd.) as a complexing agent for copper (II). The first solution was made by dissolving H_3PO_4 and pseudoboehmite in water, and the mixture was stirred for 6 h to obtain a uniform gel. Next, the second solution was prepared, which includes colloidal silica, morpholine, TEPA, $CuSO_4\cdot5H_2O$ and water, and the second solution was then slowly added to the first solution with a constant stirring. Cu/SAPO-34 samples with crystallite sizes of 1, 3, 7, 9 and 13 μm were successfully synthesized by using seed levels of 0.5, 0.1, 0.05, 0.005 and 0.0005 wt% (relative to the weight of final product), respectively. The final slurry was stirred for 6 h and subsequently transferred to a Teflon-lined stainless-steel autoclave. For all samples, crystallization was conducted at 200 °C for 48 h. After crystallization, the solid product was

centrifuged, washed with deionized water and filtered. Finally, the obtained product was dried at 120 °C for 12 h and calcined in a muffle furnace with air at 650 °C for 6 h. In addition, three H/SPAO-34 reference samples, with crystallite sizes of 3, 7 and 13 μm, were prepared using a similar procedure but with the exclusion of TEPA and Cu-$SO_4\cdot5H_2O$ in the second solution. The corresponding quantities of SAPO-34 crystal seeds used were 0.1, 0.05, 0.0005 wt%, respectively.

The fresh Cu/SAPO-34 catalysts with different crystal sizes were hydrothermally treated at 70 °C with 80% relative humidity for 96 h (LHT) in a low temperature humidity chamber (Tianyu experimental instrument co., LTD,). The H/SAPO-34 samples were treated under the same conditions but only for 3 h. After the LHT treatment, the samples were dried at 150 °C for 1 h. In this work, fresh Cu/SAPO-34 catalysts are denoted as F-Cu-X and the low-temperature hydrothermally treated Cu/SAPO-34 catalysts as LHT-Cu-X, where, X is crystallite size. Similarly, the fresh and the LHT H/SAPO-34 samples are named as F-H-X and LHT-H-X, respectively.

2.2. Characterization

The cooper contents of Cu/SAPO-34 catalysts were analyzed by inductively coupled plasma and atomic emission spectrometry (ICP-AES). Si, P and Al concentrations were measured by X-ray fluorescence (XRF) spectroscopy.

Scanning electron microscope (SEM) images were taken using a HITACHI S4800 field emission microscope. Prior to scanning, a sample was pasted on a carbon tape and then covered with an Au film for better electrical conductivity. Energy dispersive spectroscopy (EDS) was also performed during the SEM experiments to map the distributions of Si, Al and P on the surfaces of Cu/SAPO-34 and H/SAPO-34 crystals.

In addition, a line-profile of element distribution was performed on a cross section of F-Cu-13 using SEM-EDS. F-Cu-13 sample was first embedded in a piece of polymer resin using a NAIBO LHM-1000 Metallographic specimen mosaic machine. Then, the resin block was mechanically polished using ultrafine abrasive materials with a machine using a NAIBO LAP-2X Metallographic polishing machine. This polishing process cuts away about 6 μm (estimated value) of the crystal depth and exposes a cross section area within F-Cu-13 crystal. The sample preparation process is schematically illustrated in Fig. S1. Elemental compositions were measured on the cross section of a single crystal along a line from one side to the other passing through the center.

X-ray photo-electron spectroscopy (XPS) experiments were performed on all fresh Cu/SAPO-34 catalysts using an ESCALAB 250 XI spectrometer equipped with Al Kα as X-ray source (1486.6 eV), which would result in an average sample penetration depth of 4.5 nm. C 1 s at 284.6 eV was used as the standard, and the binding energy error was within ± 0.2 eV.

X-ray powder diffractograms (XRD) were collected with a 2θ step size of 0.02° from 5° to 45° at room temperature using Cu Kα as a radiation source (Bruker D8 Advance TXS, λ = 1.5418 Å). Relative crystallinity of a sample is defined as the normalized total area of five peaks (201, 003, 211, 104, 220) relative to that of F-Cu-7.

An automatic micropore physisorption analyzer (Micromeritics ASAP 2460) was used to measure micropore surface area, micropore volume and pore size of the samples using N_2 adsorption–desorption at $T = 77$ K. Prior to the tests, samples were degassed at 300 °C for 12 h under 0.133 Pa.

^{27}Al, ^{29}Si and ^{31}P MAS NMR measurements were conducted on a Varian Infinity plus 300WB spectrometer at resonance frequencies of 78.13, 59.57, and 121.37 MHz, respectively. Both ^{27}Al and ^{31}P MAS NMR spectra were recorded with a spinning rate of 8 kHz, whereas ^{29}Si spectra were collected with a spinning rate of 4 kHz. Before the measurements, all samples were dehydrated at 150 °C for 3 h.

Diethylamine, with its kinetic diameter larger than the pore opening of CHA cages, was used to probe the acidity of the exterior surface of
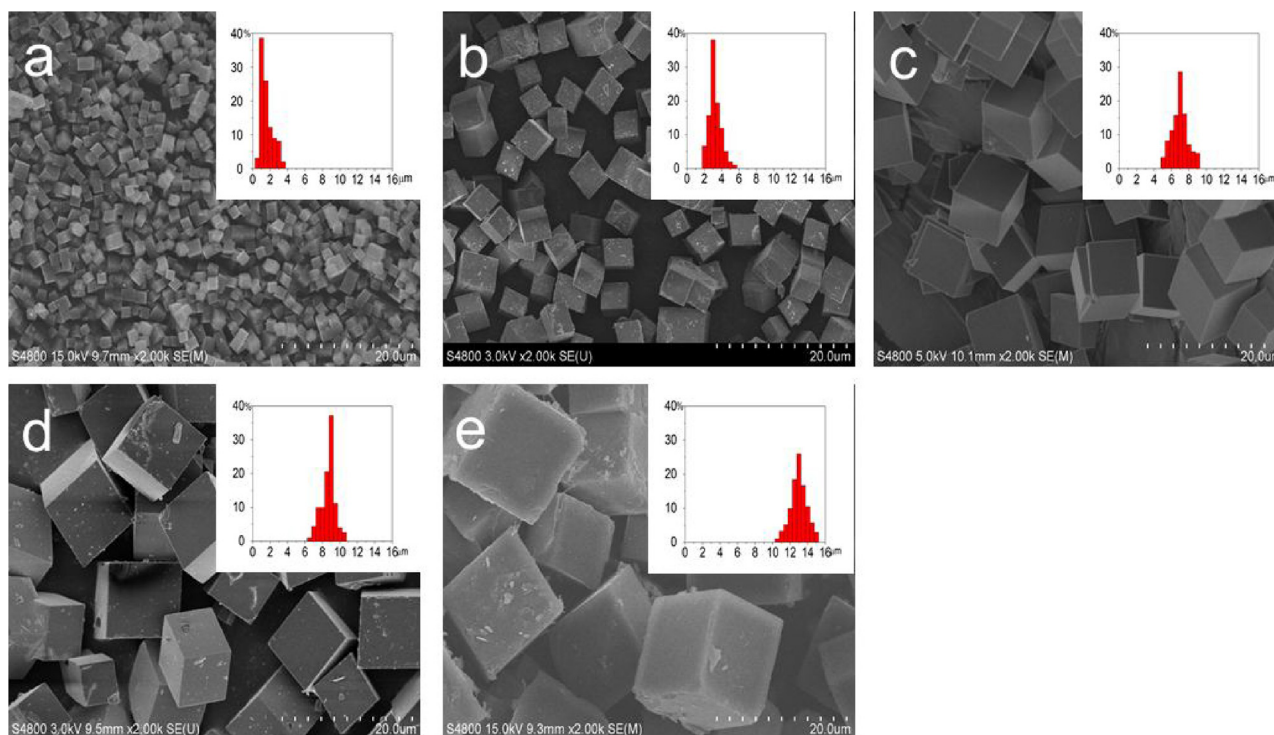
Fig. 1. SEM images of the Cu/SAPO-34 catalysts: a. F-Cu-1; b. F-Cu-3; c. F-Cu-7; d. F-Cu-9; e. F-Cu-13. The crystallite size distribution was constructed by counting about 200 crystallites randomly from SEM images.

Cu/SAPO-34 crystals. The surface acidity of the fresh Cu/SAPO-34 catalysts was measured by temperature programmed desorption (TPD) of diethylamine as a function of crystallite size. Prior to the tests, all samples were oxidized at 500 °C for 30 min with a flow of 10% O_2/N_2 and subsequently cooled down to 200 °C in pure N_2. For diethylamine adsorption, a sample was exposed to a flow of 1000 ppm diethylamine/ N_2 until saturation. The sample was then purged with a N_2 stream for 2 h to remove the weakly adsorbed diethylamine. Finally, the sample was heated from 200 °C to 600 °C at a ramp rate of 10 °C/min in flowing N_2. A MKS MultiGas 2030 FT-IR analyzer was used to measure the diethylamine concentration as a function of time/temperature. Specific surface acidity (mmol/m^2) of a catalyst was obtained by normalizing the cumulative desorption of diethylamine (mmol/g) by the geometric surface area (m^2/g) of that catalyst.

NH$_3$ temperature programmed desorption (NH$_3$-TPD) experiments were carried out to measure the bulk acidity of these samples. The experimental process is similar to diethylamine TPD experiment with a few exceptions. For NH$_3$ adsorption, the samples were exposed in the flow of 500 ppm NH$_3$/N$_2$ to reach saturation at 80 °C. After a long N$_2$ purge, the temperature was ramped from 80 °C to 600 °C at a heating rate of 10 °C min^{-1}.

Electron paramagnetic resonance (EPR) spectra were recorded on a Bruker EMXPLUS10/12. Powder samples (~ 85 mg) were contained in the quartz tubes for the EPR measurement. The X-band (ν = 9.78 GHz) was recorded at room temperature in vacuum, and the magnetic field was swept from 2000 G to 4000 G. All the EPR spectra of Cu/SAPO-34 catalysts were obtained at -150 °C.

Temperature-programmed reduction by H$_2$ (H$_2$-TPR) experiments were conducted to characterize the reducibility of various copper species in Cu/SAPO-34 catalysts. A 30 mg sample was pre-treated at 500 °C with a flow of 5% O_2/N_2 for 30 min and then cooled down to 50 °C in a N_2 stream. Finally, the sample was heated from 50 °C to 850 °C at a ramp rate of 10 °C min^{-1} with a flow of 5% H_2/N_2. H_2 consumption was recorded by a thermal conductivity detector (TCD) as a function of time/temperature. CuO powder (99%, Tianjin Kemiou Chemical Co.) was used as a quantitative reference to calibrate the TCD.

2.3. Kinetic measurements

NH$_3$ selective catalytic reduction (NH$_3$-SCR) kinetic tests were performed in a differential quartz tube reactor using 25 mg catalysts (80–100 mesh) mechanically mixed with 75 mg quartz sands (80–100 mesh). Catalysts bed temperature was controlled by an inserted K-type thermocouple. Inlet gas compositions were controlled by mass flow controllers, and outlet concentrations of NO, NO$_2$, N$_2$O and NH$_3$ were measured by a MKS MultiGas 2030 FT-IR analyzer with a 5.11-m gas cell. The reaction conditions were carefully chosen to ensure that the reaction rate was kinetically controlled (Fig. S2). The reaction temperature for the NH$_3$-SCR reaction was controlled between 150 °C and 230 °C at a 20 °C increment. The total flow rate was 1.5 L·min^{-1}, corresponding to a volume hourly space velocity (VHSV) of 3 600 000 h^{-1}. The reaction system under this condition was proved to be free of any external mass diffusion control. The reaction feed gas consisted of 500 ppm NO, 500 ppm NH$_3$, 5% O$_2$ and 5% H$_2$O with N$_2$ as the balance. A sample was first pre-oxidized in 5% O$_2$/N$_2$ at 500 °C for 30 min and then cooled down to the target reaction temperature. Steady-state NO$_x$ conversions were measured at constant temperatures after stabilization for at least 1 h.

The NH$_3$-SCR reaction rate was calculated from the NO$_x$ conversion based on Eq. (1)

$$rate\,[mol\,NO_x \bullet g_{cata}^{-1} \bullet s^{-1}] \;=\; \frac{X_{NOx}\,[\%] \;\times\; F_{NOx}\,[L_{(NOx)} \bullet min^{-1}]}{m_{catal}\,[g] \;\times\; 60\,[s \bullet min^{-1}] \;\times\; 22.4\,[L \bullet mol^{-1}]}$$

(1)

where X_{NOx} stands for NO$_x$ conversion; F_{NOx} is NO$_x$ flow rate; and m_{catal} is catalyst mass.

3. Results

3.1. Morphology, framework type and composition

Fig. 1 shows the SEM images of the fresh Cu/SAPO-34 samples. All five samples show a cubical morphology with an average crystallite
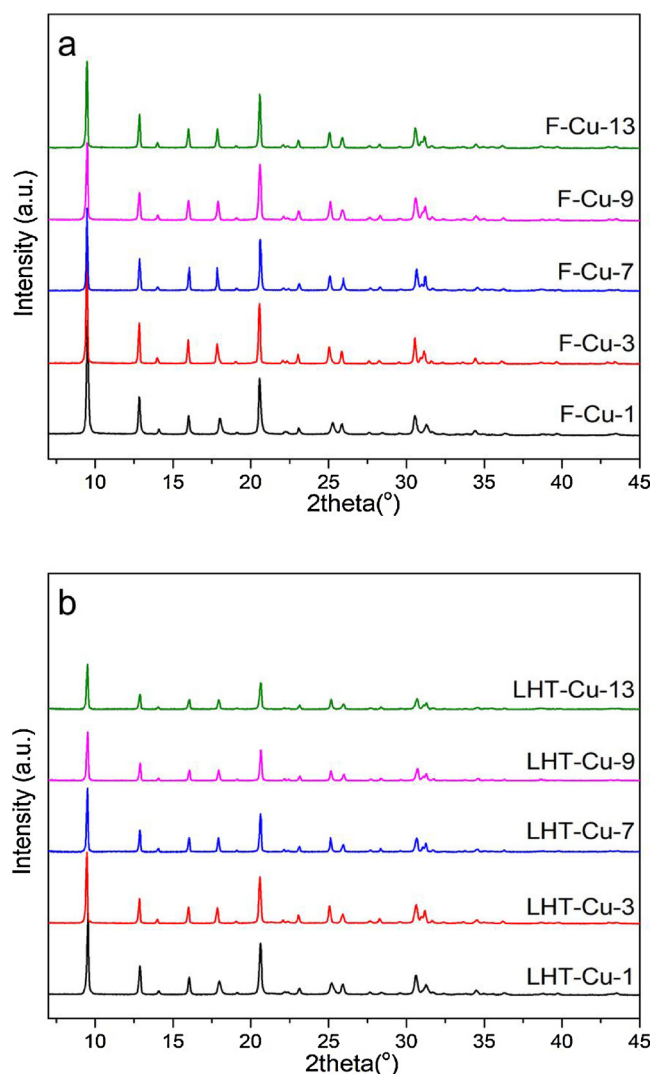
Fig. 2. XRD patterns of the Cu/SAPO-34 catalysts: a. Fresh samples; b. LHT samples.

Table 1
The average crystallite size and chemical compositions of the fresh Cu/SAPO-34 catalysts.

Sample	The average particle size (μm)	Molar composition	Cu loading (wt.%)
F-Cu-1	1.3	$Si_{0.14}P_{0.41}Al_{0.45}O_2$	4.0
F-Cu-3	3.4	$Si_{0.14}P_{0.41}Al_{0.45}O_2$	4.0
F-Cu-7	7.3	$Si_{0.15}P_{0.40}Al_{0.45}O_2$	4.1
F-Cu-9	8.9	$Si_{0.14}P_{0.40}Al_{0.46}O_2$	4.1
F-Cu-13	13.1	$Si_{0.14}P_{0.41}Al_{0.45}O_2$	4.1

sizes from 1 to 13 μm (see inserted graphs). The powder XRD patterns of these samples (Fig. 2a) confirm that they are fully formed crystalline SAPO-34 (CHA framework type) without any impurity. The ICP and XRF results show that all samples have the same chemical composition (Table 1).

3.2. Elemental distribution

Fig. 3 shows SEM-EDS line profiling results for Al, P, Si and Cu on a cross section of F-Cu-13 crystal. Because the profiling was performed on a "Cut-off" crystal, the elemental compositions are presented as a function of probing location relative to one crystal surface. The distributions of Si, P, Al and Cu were found to be non-uniform from the center to the exterior surface. P and Al concentrations are clearly lower near the crystal surface relative to the center. Si, on the other hand, had the highest concentration near the surface and lowest at the center, with a surface to center ratio of > 2. This suggests that the rate of Si incorporation is not uniform; more Si was incorporated into framework at the late stage of the crystallization process. Since Brønsted acidity in SAPO-34 is originated by replacing a P atom with a Si atom, a higher surface Si concentration implies a higher surface Brønsted acidity. However, it is difficult to detect a clear trend for Cu distribution, except that the Cu concentration on the external surface seems to be lower than that in the interior.

SEM EDS-mapping was performed on five fresh Cu/SAPO-34 samples of different crystallite sizes. The Al, P and Si concentrations obtained on these five catalysts are shown in Table 2. Based on the bulk elemental analysis (XRF), the Si concentrations of these 5 samples are about the same (14.2% with a mean absolute deviation of 0.2%). However, the average Si concentration of a sample measured by SEM-EDS monotonically increases with the crystallite size, and this increase is leaner up to 9 μm. Since the penetration depth of the EDS measurement is about 1 μm and the samples sizes are from 1 to 13 μm, the EDS results reflect the element concentrations within a thin shell near the crystal surface. Thus, the EDS data clearly suggest that Si is enriched on the surface on larger crystals. Because the Brønsted acidity can only be introduced by Si, these results also imply that the samples with larger crystallite size would show higher surface acidity.

As shown in Table 3, the surface Si concentration of every sample, including F-Cu-1, is higher than its averaged bulk Si concentration (14%), and the surface Si enrichment is more pronounced on larger crystals. This surface Si concentration measured by XPS shows a steeper dependence on crystallite size than that by SEM-EDS; this is because that XPS is more surface sensitive than EDS with a penetration depth of 4–5 nm. The shapes of the Cu 2p XPS spectra are similar for the five samples (Fig. S3). Cu $2p_{3/2}$ peaks and the typical shake-up satellite at 943.0 eV are found on these samples. Because Cu^+ and Cu° species do not have a satellite peak, this feature is used to distinguish Cu^{2+} from Cu^+ and Cu° species [8,26]. The Cu $2p_{3/2}$ peaks were deconvoluted to separate CuO species and Cu^{2+} ions. The peak at 933.3 eV is attributed to CuO species, and the peak at 935.6 eV is assigned to the isolated Cu^{2+} ions coordinated to the superficial oxygen atoms in zeolite [25,27–29]. These copper species were further quantified (in wt%) and shown in Table 3. The bulk Cu contents analyzed by ICP for all fresh samples are very similar (~4 wt%). The surface concentration of combined Cu species (CuO + Cu^{2+}) is much lower (< 1/2) than the bulk Cu concentration for all the fresh samples, and the surface copper deficiency is more obvious on large crystallite samples. This observation is consistent with the EDS line profiling results performed on F-Cu-13 (Fig. 3). In addition, on all samples, the surface isolated Cu^{2+} ions represent 50–60% of the total surface Cu species. Our previous study reported that the isolated Cu^{2+} ions played an important role in stabilizing SAPO-34 framework and minimizing the low-temperature deactivation of Cu/SAPO-34 catalysts. Therefore, merely from the perspective of surface Cu^{2+} species, one would predict that the exterior part of larger crystallite samples would be less stable compared to that of small crystallite samples.

3.3. Structural stability

Table 4 shows the nitrogen adsorption/desorption measurements for fresh and low-temperature hydrothermally treated (LHT) Cu/SAPO-34 catalysts. All fresh catalysts show similar micropore surface areas (698–709 m²/g) and micropore volumes (0.26 – 0.27 cm³/g). However, after the LHT treatment, the micropore surface area is reduced on all catalysts (662–528 m²/g), and the degree of the reduction is linearly proportional to the crystallite size. A similar trend was observed for micropore volume, albeit at a smaller degree. Interestingly, the average
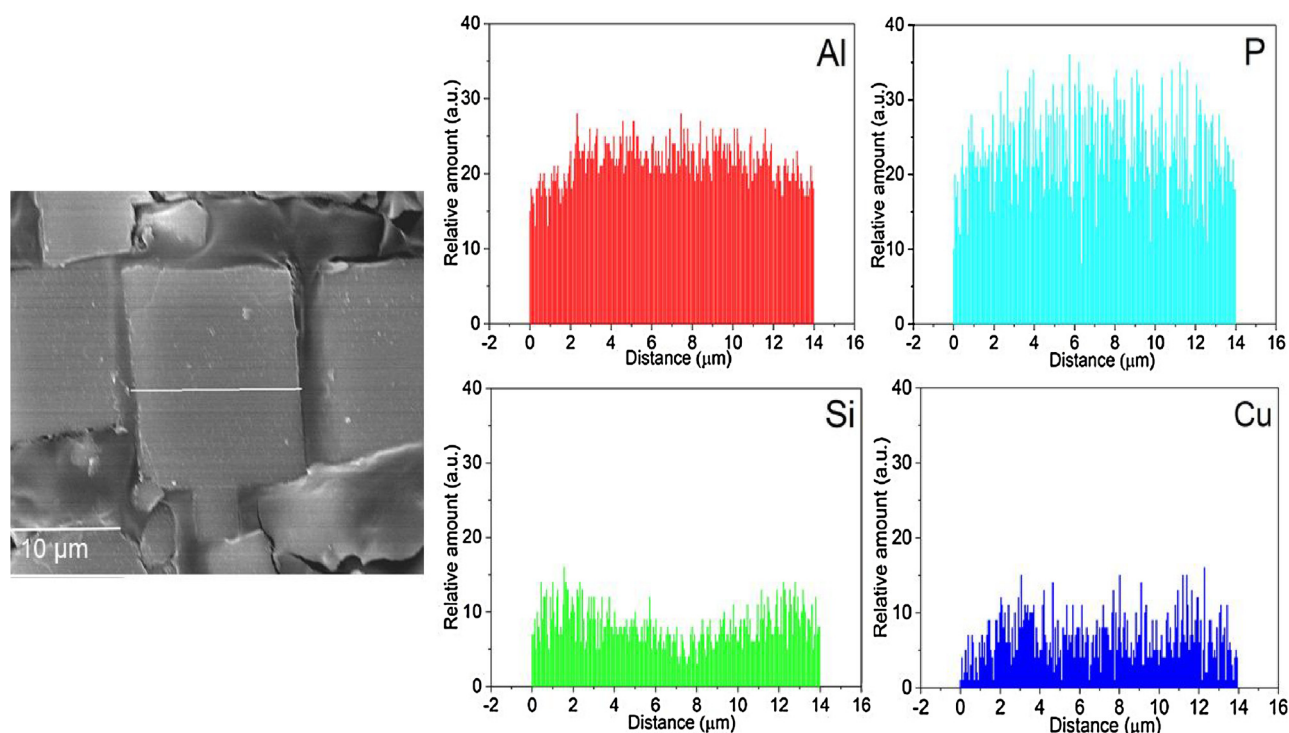
Fig. 3. SEM images and EDS-lining on the cross section of F-Cu-13 crystal.

Table 2
Elemental compositions obtained from SEM-EDS analysis of the Cu/SAPO-34 catalysts.

Samples	Al (mol %)	Si (mol %)	P (mol %)	Average surface Si content (mol%)[a]	Average bulk Si content (mol%)[b]
F-Cu-1	47.1	14.6	38.3	14.4	14.1
	47.3	14.4	38.3		
	46.6	14.3	39.1		
F-Cu-3	47.5	15.1	37.4	15.1	14.0
	46.1	14.9	39.0		
	46.5	15.2	38.3		
F-Cu-7	44.1	16.4	39.5	16.4	14.6
	46.1	16.3	37.6		
	47.3	16.4	36.3		
F-Cu-9	45.1	17.3	37.6	17.1	14.3
	45.1	16.8	38.1		
	44.7	17.1	38.2		
F-Cu-13	47.2	17.6	35.2	17.5	14.1
	46.8	17.7	35.5		
	44.1	17.3	38.6		

[a] Average surface Si contents are calculated from the SEM-EDS results.
[b] Average bulk Si contents are calculated from the XRF results.

Table 3
Si, P, Al and Cu compositions from XPS analysis.

Samples	Si (mol%)	Al (mol%)	P (mol%)	Cu^{2+} (wt%)[a]	CuO (wt%)[a]
F-Cu-1	20.06	31.60	47.45	1.00	0.89
F-Cu-3	21.27	33.48	44.99	0.80	0.61
F-Cu-7	28.46	29.68	41.22	0.74	0.64
F-Cu-9	33.12	24.84	41.41	0.62	0.46
F-Cu-13	33.34	24.85	41.09	0.67	0.48

[a] To conveniently compare the concentrations of the surface Cu species with the bulk Cu species (ICP results), wt% is used as the unit.

pore size remained unchanged (0.37–0.38 nm). As shown in Fig. 2b and Table 4, the low-temperature hydrothermal treatment also resulted in the loss of relative crystallinity compared with the corresponding fresh

Table 4
The texture properties of Cu/SAPO-34 catalysts.

Samples	Pore size (nm)	Micropore volume (cm^3/g)	Micropore surface area (m^2/g)	Relative crystallinity (%)
F-Cu-1	0.378	0.26	698	96
F-Cu-3	0.374	0.27	702	99
F-Cu-7	0.374	0.26	699	100
F-Cu-9	0.375	0.27	707	95
F-Cu-13	0.376	0.26	709	93
LHT-Cu-1	0.375	0.26	662	76
LHT-Cu-3	0.381	0.24	641	72
LHT-Cu-7	0.376	0.24	609	59
LHT-Cu-9	0.373	0.23	579	46
LHT-Cu-13	0.374	0.21	528	42

catalyst, and again the sample with the largest crystallite size (LHT-Cu-13) suffered the most, lost ˜60% its relative crystallinity.

Solid-state MAS NMR was used to probe the local structure of the framework Si, P, and Al. Fig. 4a shows the ^{27}Al MAS NMR spectra. A single peak was found on all five fresh catalysts centered at 32.8 ppm, ascribing to the tetrahedral Al (Al^{IV}) [30]. After the LHT, a new peak appeared around −11.8 ppm on all the catalysts, which are attributed to the octahedral Al (Al^{VI}), and this peak appears to increase with crystallite size [30]. On LHT-Cu-13, an additional chemical shift at 12.4 ppm was detected, which may be assigned to the pentahedral Al (Al^{V}) [31,32]. The formation of Al^{VI} and Al^{V} suggests that the LHT has destroyed some Si−O−Al bonds in the Cu/SAPO-34 structure, and the degree of destruction is proportional to the crystallite size of the catalyst. The ^{27}Al MAS NMR results are consistent with the XRD and BET results that show the loss of crystallinity and micropore surface area due to LHT is directly related to crystallite size. Fig. 4b shows the ^{31}P MAS NMR spectra of fresh and LHT Cu/SAPO-34 catalysts. On all fresh catalysts, a single peak was observed at −29.5 ppm and is assigned to the tetrahedral P in the SAPO-34 framework [32]. On the LHT catalysts, the intensity of the peak at −29.5 ppm is found to decrease with increasing crystallite size, while the peak width (FWHM) increases with
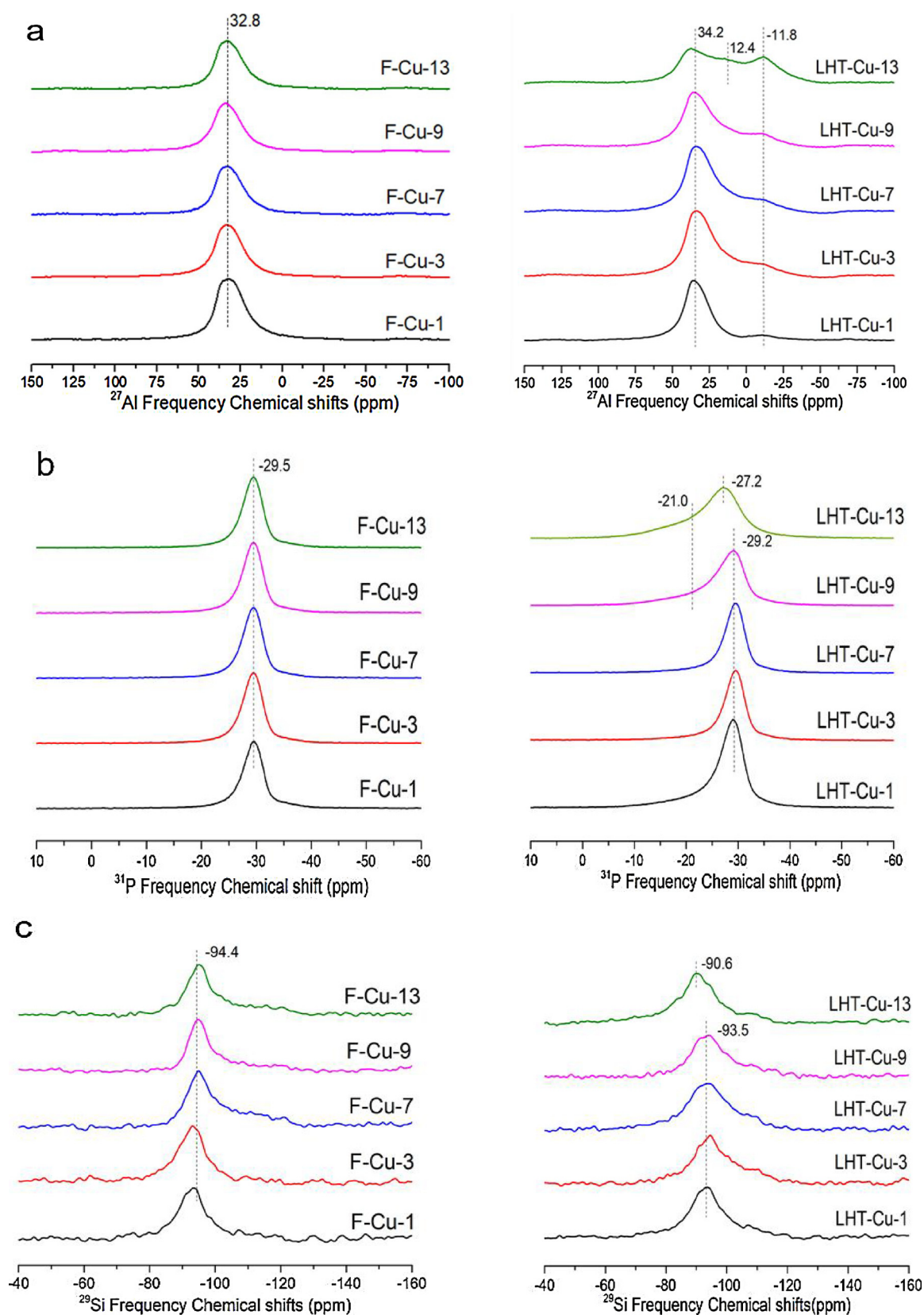
Fig. 4. NMR spectra of the Cu/SAPO-34 catalysts before and after the hydrothermal treatment: a. ^{27}Al; b. ^{31}P; c. ^{29}Si.

the crystallite size. In addition, a new signal was found at −21.0 ppm on LHT-Cu-9 and LHT-Cu-13, which is due to phosphorus atoms coordinated with H_2O molecules [30]. The change in peak shape on catalysts with larger crystallites is likely due to the deterioration of the

SAPO-34 framework caused by the LHT. Fig. 4c depicts the ^{29}Si MAS NMR spectra of fresh and LHT Cu/SAPO-34 catalysts. A single peak appears around −94.4 ppm on all fresh catalysts, which is attributed to the isolated Si (Si(OAl)$_4$ species). On the LHT catalysts, this peak is

shifted to −90.6 ppm on LHT-Cu-13 and to −93.5 ppm on the other LHT catalysts [23,30,31,33]. It infers that the chemical state of Si species is mainly in the form of isolated Si. Compared with the fresh samples, LHT samples present broadened Si signals. As a result, an occurrence of amorphous silicon complexes induced by Si-O-Al bonds cleavage [34].

The acidity of SAPO-34 molecular sieve is generated by the Si-O-Al linkage, which is the result of substituting a P atom by a Si atom in the AlPOs framework [35–37]. The ^{29}Si NMR results show that most of the Si species in all fresh Cu/SAPO-34 catalysts are isolated Si atoms. Thus, the Si distribution should represent may be equivalent to the distribution of Si−O−Al bonds in a Cu/SAPO-34 crystal.

3.4. Brønsted acid sites distribution

Pyridine-FTIR is one of effective method to qualitatively characterize the surface acidity of materials [38]. In this study, we attempted to conduct pyridine-FTIR to investigate the external surface acidity of Cu/SAPO-34 catalysts. Because the 8-ring window of SAPO-34 structure is much smaller than the kinetic diameter of pyridine (4.3 vs 5.9 Å), pyridine molecules cannot penetrate the cavities of SAPO-34 and can only interact with those hydroxyl groups at the external surface of the crystallites. As shown in Fig. S4, two negative bands at 1542 and 1447 cm^{-1} assigned as the Brønsted acid sites and Lewis acid sites [39,40]. With decreasing the crystallite size, these two negative bands gradually decrease, indicating the amount of external surface acid sites is lower on smaller crystals. The signal of F-Cu-1 is very weak, probably because the amount of pyridine adsorption on the external surface of F-Cu-1 crystallites were too low to identify.

To quantitatively characterize the external surface acidity and bulk acidity of Cu/SAPO-34 catalysts, TPD experiments with diethylamine and NH$_3$ were carried out. Since the cross sections of diethylamine and n-pentane are similar, the kinetic diameter of diethylamine is believed to be similar to that of n-pentane (4.5 Å) as well [41], which is larger than the opening of the 8-member rings in CHA structure (4.3 Å) [42]. Therefore, diethylamine-TPD measures the acidity on the external surface of the Cu/SAPO-34 catalysts. As shown in Fig. 5a, a relatively broad diethylamine desorption peak appears around 407 °C on all fresh Cu/SAPO-34 catalysts, and the peak intensity increases with crystallite size. This peak is assigned to the adsorption of diethylamine on the Brønsted acid sites on the external surface of Cu/SAPO-34. When normalized by the external surface area (geometric surface area (m²/g)) of the crystals, the difference in diethylamine adsorption is even more dramatic. As shown in Fig. 5b, the surface acid site density, in mmol/m², increases exponentially with crystallite size, with F-Cu-13 being 55 times that of F-Cu-1. This may be due to the combination of higher Si-O-Al density (Tables 2 and 3) and lower Cu concentration (Fig. 3 and Table 3) on the exterior surfaces of large crystals.

NH$_3$-TPD was used to evaluate the acidity of the bulk catalysts because NH$_3$ is small enough (kinetic diameter = 2.9 Å) to access any location within the CHA structure. Fig. S5 shows the NH$_3$-TPD profiles of all fresh and LHT Cu-SAPO-34 catalysts. Three desorption peaks were observed, which are related to three different types of acid sites. The desorption peak around 146–158 °C is assigned to the surface hydroxyl groups (peak A). The peak around 230–240 °C is attributed to the weak structural Brønsted acid sites (peak B). The peak around 312–330 °C is ascribed to the strong structural Brønsted acid sites and Lewis acid sites created by Cu^{2+} species (peak C) [17,18]. Table 5 shows the quantities of different acid sites on all fresh and LHT catalysts calculated from the NH$_3$-TPD deconvoluted curves. On all fresh catalysts, the total acid quantities as well as the ratios among different types of acid sites are similar, independent of crystallite size. This is because they all have the same bulk chemical compositions (Table 1). After the LHT, the amounts of both Brønsted acid sites and Lewis acid sites were found to decrease, and the extent of the decrease is proportional to the crystallite size of the catalyst. The NH$_3$-TPD results are entirely consistent with the XRD
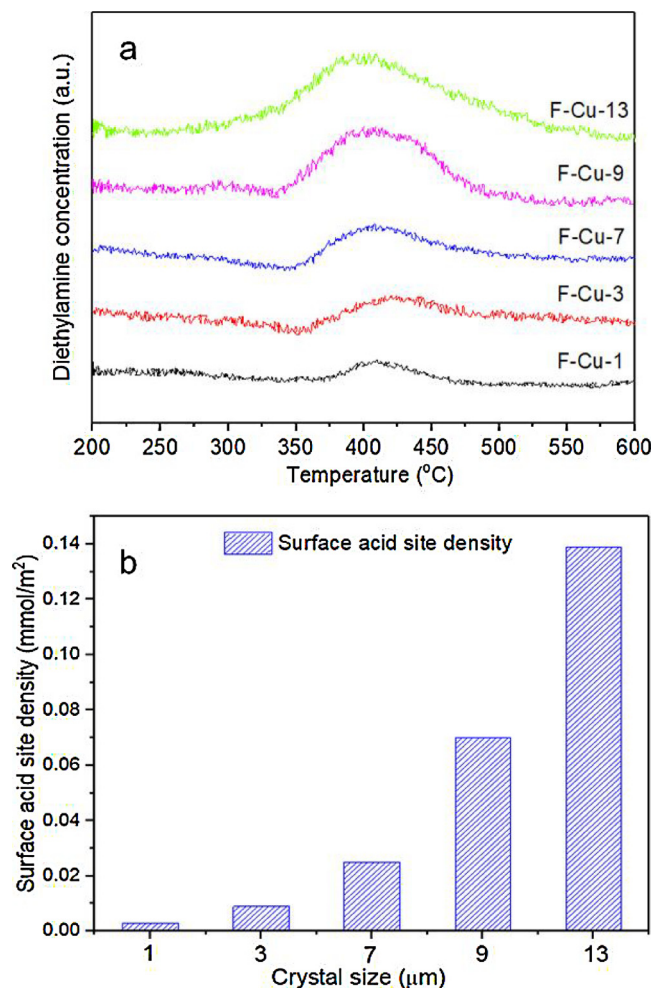

Fig. 5. a: Diethylamine TPD results of fresh Cu/SAPO-34 catalysts; b: Surface acid site density of fresh Cu/SAPO-34 catalysts as a function of crystallite size. The acid site density is based on the diethylamine TPD measurement and normalized by the geometric external surface area of Cu/SAPO-34.

Table 5
NH$_3$ released at different temperatures of all the catalysts obtained from NH$_3$ TPD (mmol/g$_{catal.}$).

Samples	Total NH$_3$ storage	Peak		
		A 146-158 °C	B 230-240 °C	C 312-330 °C
F-Cu-1	1.216	0.139	0.334	0.741
F-Cu-3	1.190	0.130	0.329	0.731
F-Cu-7	1.191	0.139	0.329	0.724
F-Cu-9	1.188	0.134	0.326	0.728
F-Cu-13	1.189	0.130	0.328	0.731
LHT-Cu-1	1.161	0.123	0.316	0.722
LHT-Cu-3	1.033	0.092	0.276	0.665
LHT-Cu-7	0.905	0.086	0.247	0.572
LHT-Cu-9	0.804	0.081	0.235	0.488
LHT-Cu-13	0.765	0.080	0.215	0.470

and BET results; the structure integrity of LHT Cu/SAPO-34 catalyst is closely related to its crystallite size. Thus, reduction in Brønsted acid site quantity must be the result of reduction in Si-O-Al linkage and crystallinity. And the partial collapse of SAPO-34 framework lead to the reduction in Cu^{2+} species.
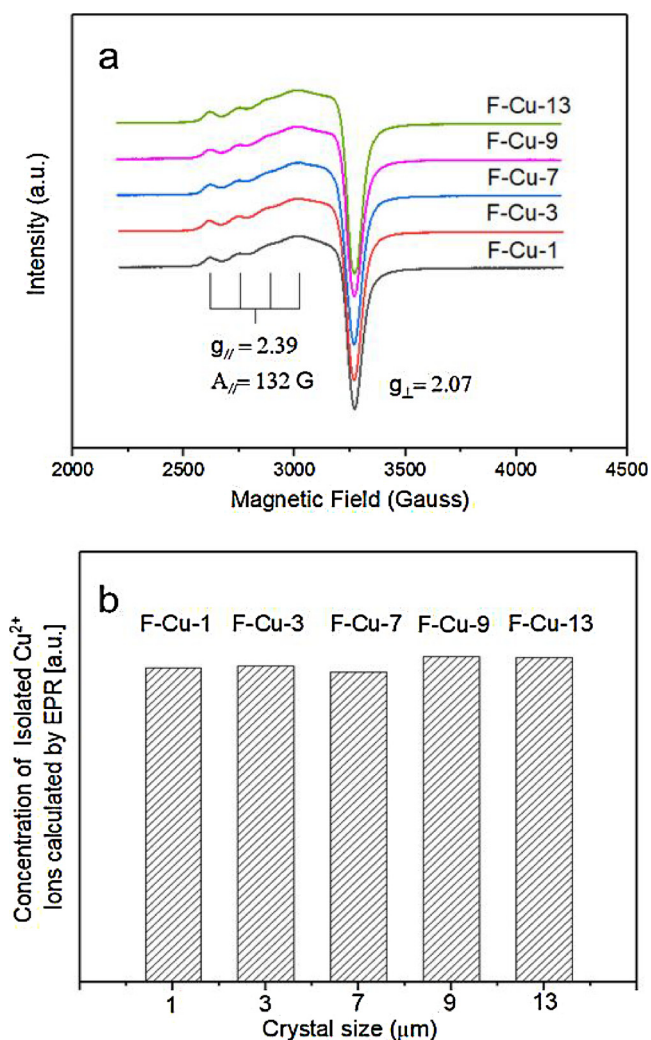
Fig. 6. a: EPR spectra of fresh Cu/SAPO-34 catalysts; b: Concentration of isolated Cu^{2+} ions as a function of crystal size semi-quantified by double integrating the EPR spectroscopy.

3.5. Cu species

Isolated Cu^{2+} ions in Cu/SSZ-13 and Cu/SAPO-34 catalysts have been demonstrated to play a key role in NH_3-SCR reaction [8]. Fig. 6a shows the EPR spectra of the five fresh Cu/SAPO-34 catalysts. All isolated Cu^{2+} ions are in identical chemical environments with $g_\parallel$ of 2.39 and $A_\parallel$ of 132 G. These values are consistent with an octahedral coordination of Cu^{2+} ions to three framework oxygen atoms and three water molecules and residing in Site (I) [43–45]. The amount of isolated Cu^{2+} ions were semi-quantified by double integrating the first-derivative EPR spectra for all fresh catalysts. Fig. 6b shows that the amounts of isolated Cu^{2+} ions in all fresh samples are very similar. Fig. S6 shows the H_2-TPR profiles of all fresh and LHT Cu/SAPO-34 catalysts. The TPR peak assignments on Cu/SAPO-34 catalysts have been established previously. The peak around 220–240 °C is assigned to the reduction of isolated Cu^{2+} ions; the peak around 280–300 °C is attributed to the reduction of copper oxides; and the peak around 600–800 °C is ascribed to the reduction of Cu^+ ions [18,46]. The quantifications of the individual copper species are listed in Table 6. The five fresh catalysts show similar amounts of isolated Cu^{2+} ions and CuO clusters, with Cu^{2+} representing 49% of the total copper species on all fresh catalysts. The identical quantity and proportion for the isolated Cu^{2+} ions on all fresh catalysts provide a sound basis to compare their NH_3-SCR activities. Interestingly, the proportion of the

Table 6
Quantitative results of each copper species coexist in Cu/SAPO-34 catalysts by H_2 TPR.

Sample	Copper species content (wt.%)	
	Isolated Cu^{2+}	Copper oxide
F-Cu-1	1.95	2.05
F-Cu-3	1.97	2.03
F-Cu-7	2.02	2.08
F-Cu-9	2.00	2.10
F-Cu-13	2.01	2.09
LHT-Cu-1	1.74	2.16
LHT-Cu-3	1.65	2.23
LHT-Cu-7	1.56	2.44
LHT-Cu-9	1.11	2.86
LHT-Cu-13	0.96	2.95

Cu^{2+} ions in the bulk is not too much different from that on the surface (53–58%) measured by XPS (Table 3), although the quantities of the total copper species are significantly lower on the surface. After the LHT, the number of isolated Cu^{2+} ions are found to decrease, and this decrease is significantly more pronounced on larger crystallite catalysts. Conversely, the quantities of the CuO clusters show an opposite trend, a result of converting Cu^{2+} ions to CuO clusters. Consequently, the proportion of the Cu^{2+} decreases with increasing crystallite size (from 45% for LHT-Cu-1 to 14% on LHT-Cu-13). This decrease in Cu^{2+} is obviously due to the partial collapse of the SAPO-34 framework.

3.6. NH₃-SCR activity

The reaction rates for NH_3-SCR were derived from the NO_x conversion data obtained under differential conditions and calculated based on Eq. (1) in a temperature range of 150–230 °C. Fig. 7 shows the Arrhenius plots for all fresh and LHT catalysts. Regardless crystallite size, all fresh catalysts show identical reaction rates with overlapping Arrhenius plots. However, much lower reaction rates are found over the LHT catalysts; the extent of the decrease is proportional to the crystallite size. The obvious reason for the decreased activity is the loss of isolated Cu^{2+} ions (Table 6) due to partial collapse of the SAPO-34 framework. Interestingly, all catalysts (fresh and LHT) show very similar apparent activation energy (Ea = 48.9 kJ/mol), suggesting that the nature of active site and reaction mechanism remain unchanged before and after the LHT. These results also indicate that the rates so
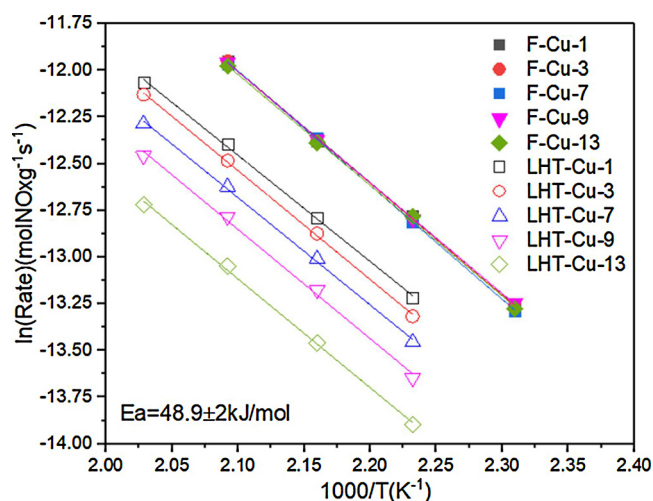

Fig. 7. Arrhenius plots of the SCR reaction rates over Cu/SAPO-34 catalysts with different crystal size. The reaction gas consisted of 500 ppm NO, 500 ppm NH_3, 5% O_2, 5% H_2O with N_2 as the balance. Flow rate: 1.5 L·min^{-1}, SV: 3 600 000 h^{-1}.
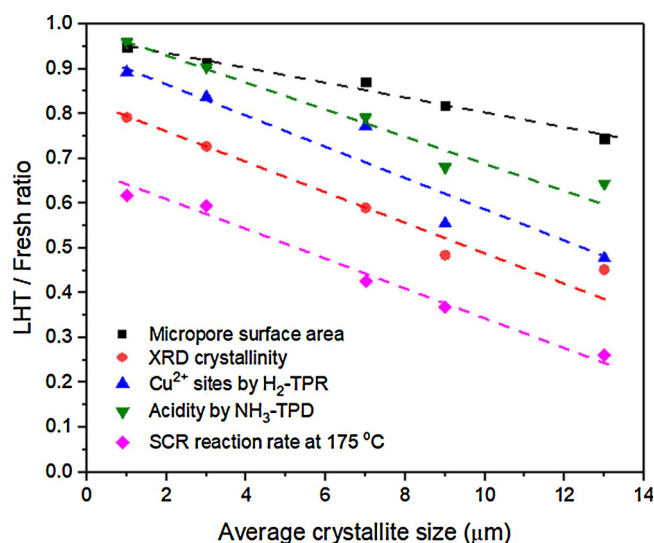
Fig. 8. The structural deterioration and rate decrease as a function of crystallite size for Cu/SAPO-34 catalysts.

Fig. 9. Surface Si content/acid sites content as a function of crystallite size.

measured are close to the intrinsic reaction rates and free of mass diffusion control.

NH$_3$ SCR activity of fresh and LHT catalysts is shown in Fig. S7 as a function of temperature. The NO conversion is identical on all fresh catalysts throughout the entire temperature range. Above 80% NO conversion is achieved between 230–500 °C. After the LHT treatment, the NO conversions decrease on all catalysts and the extent of decrease is proportional to the crystallite size. Thus, the results shown in Fig. 7 are entirely consistent with those in Fig. S7.

4. Discussion

Ordinarily, one would not suspect that crystallite size influences the low-temperature hydrothermal stability of Cu/SAPO-34. In this work, we have clearly demonstrated that crystallite size is a key parameter in this regard. As shown in Fig. 8, the impact of crystallite size on the structural integrity and bulk properties of Cu/SAPO-34 after the LHT is systematic and consistent. Except micropore surface area, the deterioration factors (LHT/Fresh) of theses bulk properties are inversely proportional to the average crystallite size with an identical slope. This suggests that the deteriorations in structural properties may be derived from a single cause.

The structural deterioration was also found on the Cu-free H/SAPO-34 materials of similar bulk compositions (see Table S1 and Fig. S8). As shown in Table S2, Fig. S9 and Fig. S10, the extent of reduction in structural properties (crystallinity, BET surface area, pore volume, acid site density) are also proportional to the crystallite size. The difference is that the deterioration on a H/SAPO-34 sample is much more severe than that on the corresponding Cu/SAPO-34 catalyst.

It is well accepted that Si-O-Al linkage is a key factor affecting the irreversible LHT hydrolysis of the SAPO-34 based catalysts [15,32]. The more severe deterioration of the H/SAPO-34 samples relative to the Cu/SAPO-34 catalysts confirms the notion that the exchanged Cu^{2+} ions can stabilize the structure [16,17]. This stabilizing effect has been discussed in detail in the Supplementary Information: a new Cu/SAPO-34 catalyst with the same crystallite size (7 μm) but different Cu content (2%Cu) was prepared (Table S3). After LHT treatment, the extent of SAPO-34 framework deterioration is inversely proportional to Cu content (Fig. S11 and Table S4). These results also reinforce the idea that Si−O−Al group is the weakest link for the structure stability.

Si-O-Al linkage is generated by Si incorporation into the AlPO-34 framework, as such the distribution of Si−O−Al linkage is determined by the Si distribution. As shown in Table S5, although the total Si
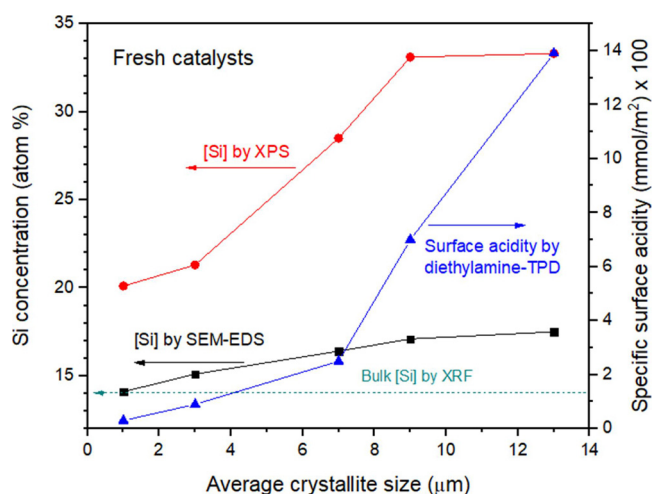
contents of all H/SAPO-34 samples are the same, the surface Si concentration is higher on the larger crystallite samples, which is similar to what was found on the Cu/SAPO-34 catalysts. Fig. 9 summarizes the surface properties of fresh Cu/SAPO-34 catalysts as a function of crystallite size, measured with techniques of different surface sensitivity. It is clear that the surface Si concentration or acidity is proportional to the average crystallite size. The proportionality is related to the surface sensitivity of the technique used (diethylamine titration > XPS > SEM-EDS). Since all catalysts have the same bulk composition, a higher surface Si concentration suggests a surface enrichment of Si. The Si gradient has been visually demonstrated by the line profile analysis of the cross section of a 13 μm Cu/SAPO-34 crystal. The same experiment also shows that Cu is not enriched on the surface. Thus, the surface enrichment of the Si−O−Al linkages should be even more pronounced, which is confirmed by the diethylamine experiment.

Since the hydrolysis of the Si−O−Al site is the fundamental cause of the structural deterioration of Cu/SAPO-34 under LHT conditions, surface enrichment of this functional group suggests that the hydrolysis would start from the surface, progressing to the bulk. Consequently, the more surface enrichment of Si−O−Al sites (the larger the crystallite size), the more vulnerable to the low-temperature hydrothermal aging. Based on this analysis, a deactivation mechanism is proposed. As displayed in Scheme 1, once the external surface Si-O-Al bonds are broken, the outer layer of the crystal is collapsed, which exposes a new surface. The newly exposed Si−O−Al linkages continue to be attacked by H$_2$O molecules, resulting in the collapse of another layer of the structure. With increasing LHT time, the structure is gradually destroyed layer-by-layer. This "layer-by-layer" mechanism is supported by the fact that it takes a long time to completely destroy the SAPO-34 framework under the low-temperature hydrothermal conditions.

So far, we have clearly established the relationship between the structural stability of a SAPO-34 based material and its crystallite size. A question arises then, why would a larger-crystallite SAPO-34 material exhibit a higher Si surface enrichment? Is this phenomenon related to preparation methodology and crystallization kinetics? In general, crystallite size is determined by the ratio of nucleation rate to growth rate. When growth rate is higher than nucleation rate, the synthesis tends to produce larger crystals, and conversely reversed conditions produce smaller crystallites. For example, supersaturation of synthesis system is used as an important method to alter the balance between these two rates. Although both growth rate and nucleation rate can increase by increasing the supersaturation, the nucleation rate increases more rapidly than the growth rate [47–49], favoring smaller crystallites. It is reported that parameters like alkalinity, crystallization temperature, the type and concentration of SDA and the amount of Si could
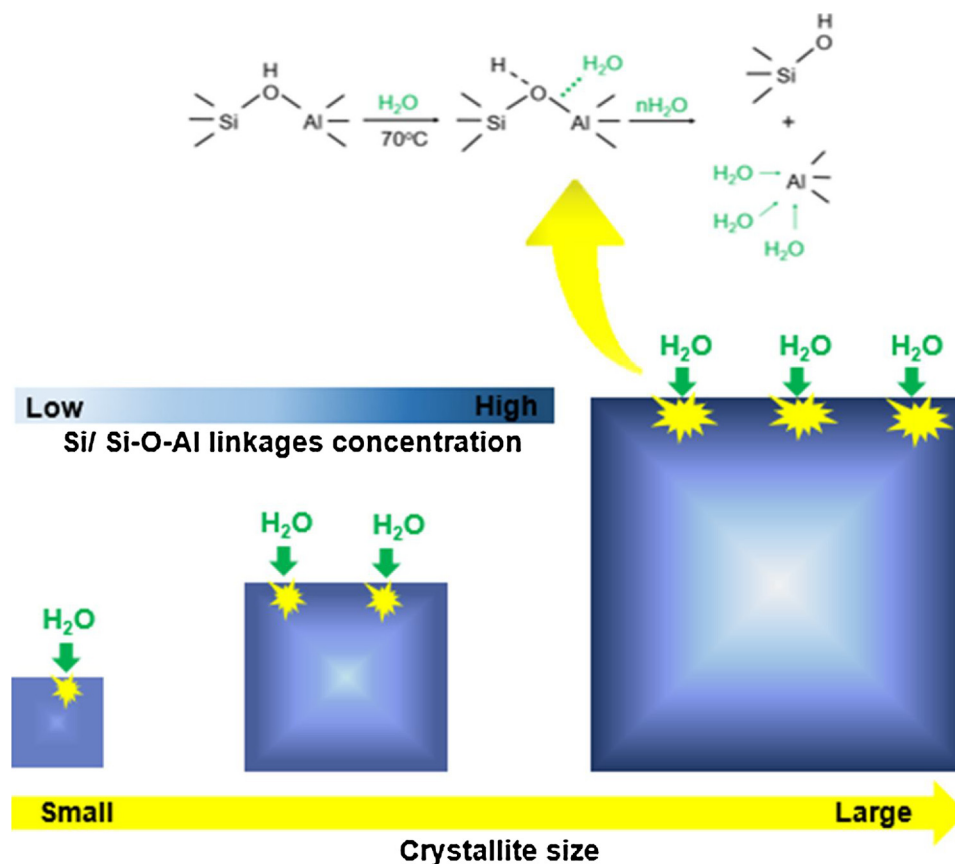
Scheme 1. The proposed deterioration mechanism of Cu/SAPO-34 with varying the crystal sizes in presence of H_2O at 70 °C.

influence the supersaturation of synthesis system and therefore the crystallite size [47,50,51]. In this study, we control the crystallite size by using various amounts of seeds with otherwise identical synthesis conditions. SAPO-34 seeds were added to the synthesis system just before the hydrothermal reaction to direct the crystallization towards the CHA structure. Adding seeds provides growth surface and increases the amount of growth units. The more seeds are added to the synthesis system, the more growth units are generated. Such a system tends to have a higher consumption rate of reactants and produce smaller crystallites. This type of synthesis conditions also tends to produce crystals with more uniform distribution of elements within crystal. As crystals grow larger, the pH value in the synthesis system increases [52]. This would strongly increase the solubility of silicate species and thereby promote the incorporation of Si into the framework. As a result, the local Si concentration towards the crystal surface is higher than that at the core. As reported by many researchers [36,37,53–55], as the crystallization time increases, the chemical conditions in the synthetic gel are constantly changing, which promotes the incorporation Si into the framework and causes surface Si enrichment. In addition, the degree of Si incorporation is dependent on the crystallization time; a large crystal requires a long crystallization time.

The nature of the crystallite size dependence can be illustrated by the Si (Si-O-Al) distribution within a crystal, which is determined by the current synthesis condition (seed level). It is likely that this conclusion is limited to this type of synthesis method, where the crystallite size is controlled by varying seeds amount. The crystals synthesized under this conditions also have: a) identical chemical composition (especially total Si content and Cu content); b) same quantity of the Brønsted acid sites; and c) same amount of the isolated Cu^{2+} ions. The latter two requirements are especially important because the amount of Brønsted acid sites and isolated Cu^{2+} ions are directly related the low-temperature hydrothermal stability of Cu/SAPO-34 catalysts. Although many

methods have been reported in literatures to control the crystal size of SAPO-34, for example using different SDAs, temperatures, dry gel etc., the regular pattern of element distribution in crystals has been rarely studied. Using different synthesis methods, the element distributions in crystals are most likely to be different. Moreover, different synthesis methods can directly affect the crystalline structure of final product. For example, if we use the same synthesis gel but different SDAs, the distribution of Si species and the amount of isolated Si (which is equivalent to the amount of Brønsted acid sites) in the final product would be different [13,56,57]. Herein, this work does suggest a set of material requirements that can lead to more stable Cu/SAPO-34 catalysts after the LHT. If using the synthesis method described in this work, smaller crystallite sizes (more seeds) are clearly preferred. Coupling of a smaller crystallite size with a higher degree of Cu^{2+} exchange would lead to a better low-temperature hydrothermal stability for Cu/SAPO-34 catalysts. In addition, "secondary crystallization" that is being investigated in our group could be another potential synthesis method. In this case, the crystals could recrystallize to form a Cu/SAPO-34 with a low Si content outer layer. On the basis of good NH_3 SCR performance, the resistance of Cu/SAPO-34 towards low temperature water steam would be further strengthened.

5. Conclusions

We examined the low-temperature hydrothermal stability of a series of Cu/SAPO-34 catalysts of identical chemical compositions but different crystallite sizes (1 to 13 μm) using a variety of characterization tools and kinetics measurements. The low-temperature hydrothermal stability of a Cu/SAPO-34 catalyst was found to be closely related to its average crystallite size. After the hydrothermal treatment (96 h at 70 °C with 80% humidity), a loss of micropore surface area, micropore volume, relative crystallinities, acidity and isolated Cu^{2+} ions were

observed on all samples, and the decrease was proportional to the average crystallite size. NH₃-SCR reaction rates suffered a similar decrease with increasing crystallite size. It was further discovered that the distribution of Si (and Brønsted acidity) on a fresh Cu/SAPO-34 catalyst was not uniform from the crystal center to its surface, and the concentration gradient was very much dependent on the crystallite size. The larger the crystallite, the more surface enrichment for Si. This surface enrichment of Si and Brønsted acidity is thought to be the root cause for the structural vulnerability found on larger crystallite catalysts under LHT conditions. This understanding is entirely consistent with the observation found on the H/SAPO-34 reference materials of the same sizes, where the structural destruction is even more severe after the LHT. Thus, fewer Si−O−Al linkages on the surface of a crystal surface would favor a lesser degree of structural collapse. Practically, a more stable Cu/SAPO-34 catalyst may be obtained by making the crystallites small with fewer surface Si-O-Al linkages. This finding could be a useful strategy to improve the structural stability of SAPO-34 framework.

Acknowledgements

Appendix A. Supplementary data

Supplementary material related to this article can be found, in the online version, at doi:https://doi.org/10.1016/j.apcatb.2019.02.054.

References

[1] S. Brandenberger, O. Kröcher, A. Tissler, R. Althoff, Catal. Rev. 50 (2008) 492–531.
[2] U. Deka, I. Lezcano-Gonzalez, B.M. Weckhuysen, A.M. Beale, ACS Catal. 3 (2013) 413–427.
[3] D.W. Fickel, E. D'Addio, J.A. Lauterbach, R.F. Lobo, Appl. Catal. B 102 (2011) 441–448.
[4] J.H. Kwak, R.G. Tonkyn, D.H. Kim, J. Szanyi, C.H.F. Peden, J. Catal. 275 (2010) 187–190.
[5] L. Ma, Y. Cheng, G. Cavataio, R.W. McCabe, L. Fu, J. Li, J. Chem. Eng. 225 (2013) 323–330.
[6] J.H. Kwak, D. Tran, S.D. Burton, J. Szanyi, J.H. Lee, C.H.F. Peden, J. Catal. 287 (2012) 203–209.
[7] J. Song, Y. Wang, E.D. Walter, N.M. Washton, D. Mei, L. Kovarik, M.H. Engelhard, S. Prodinger, Y. Wang, C.H.F. Peden, F. Gao, ACS Catal. 7 (2017) 8214–8227.
[8] L. Wang, J.R. Gaudet, W. Li, D. Weng, J. Catal. 306 (2013) 68–77.
[9] I. Tatsumi, K. Masaru, H. Fumiaki, T. Yusaku, J. Catal. 169 (1997) 93–102.
[10] K. Leistner, L. Olsson, Appl. Catal. B 165 (2015) 192–199.
[11] J. Woo, K. Leistner, D. Bernin, H. Ahari, M. Shost, M. Zammit, L. Olsson, Catal. Sci. Technol. 8 (2018) 3090–3106.
[12] R. Vomscheid, M. Briend, M.J. Peltre, P. Massiani, P.P. Man, D. Barthomeuf, Chem. Commun. 6 (1993) 544–546.
[13] M. Briend, R. Vomscheid, M.J. Peltre, P.P. Man, D. Barthomeuf, J. Phys. Chem. 99 (1995) 8270–8276.
[14] J.C. Poshusta, R.D. Noble, J.L. Falconer, J. Membr. Sci. 186 (2001) 25–40.
[15] F.D.P. Mees, L.R.M. Martens, M.J.G. Janssen, A.A. Verberckmoes, E.F. Vansant, Chem. Commun. 1 (2003) 44–45.
[16] Y. Cao, D. Fan, P. Tian, L. Cao, T. Sun, S. Xu, M. Yang, Z. Liu, J. Chem. Eng. 354 (2018) 85–92.
[17] J. Wang, D. Fan, T. Yu, J. Wang, T. Hao, X. Hu, M. Shen, W. Li, J. Catal. 322 (2015) 84–90.
[18] X. Hu, M. Yang, D. Fan, G. Qi, J. Wang, J. Wang, T. Yu, W. Li, M. Shen, J. Catal. 341 (2016) 55–61.
[19] W. Dai, G. Wu, L. Li, N. Guan, M. Hunger, ACS Catal. 3 (2013) 588–596.
[20] N. Nishiyama, M. Kawaguchi, Y. Hirota, D.V. Vu, Appl. Catal. A 362 (2009) 193–199.
[21] A.M. Prakash, S. Unnikrishnan, J. Chem. Soc. Faraday Trans. 90 (1994) 2291–2296.
[22] J.Y. Luo, H. Oh, C. Henry, W. Epling, Appl. Catal. B 123-124 (2012) 296–305.
[23] F. Gao, E.D. Walter, N.M. Washton, J. Szanyi, C.H.F. Peden, Appl. Catal. B 162 (2015) 501–514.
[24] L. Ren, L. Zhu, C. Yang, Y. Chen, Q. Sun, H. Zhang, C. Li, F. Nawaz, X. Meng, F.-S. Xiao, Chem. Commun. 47 (2011) 9789–9791.
[25] R. Martínez-Franco, M. Moliner, C. Franch, A. Kustov, A. Corma, Appl. Catal. B 127 (2012) 273–280.
[26] T. Zhang, J. Li, J. Liu, D. Wang, Z. Zhao, K. Cheng, J. Li, AIChE J. 61 (2015) 3825–3837.
[27] H. Zhao, H. Li, X. Li, M. Liu, Y. Li, Catal. Today 297 (2017) 84–91.
[28] Y. Wang, A.V. Biradar, G. Wang, K.K. Sharma, C.T. Duncan, S. Rangan, T. Asefa, Chemistry 16 (2010) 10735–10743.
[29] P.N.R. Venneström, A. Katerinopoulou, R.R. Tiruvalam, A. Kustov, P.G. Concepcion, A. Corma, ACS Catal. 3 (2013) 2158–2161.
[30] A. Buchholz, W. Wang, A. Arnold, M. Xu, M. Hunger, Microporous Mesoporous Mater. 57 (2003) 157–168.
[31] J. Wang, H. Zhao, G. Haller, Y. Li, Appl. Catal. B 202 (2017) 346–354.
[32] F. Gao, Y. Wang, N.M. Washton, M. Kollár, J. Szanyi, C.H.F. Peden, ACS Catal. 5 (2015) 6780–6791.
[33] L. Xu, A. Du, Y. Wei, Y. Wang, Z. Yu, Y. He, X. Zhang, Z. Liu, Microporous Mesoporous Mater. 115 (2008) 332–337.
[34] J. Tan, Z. Liu, X. Bao, X. Liu, X. Han, C. He, R. Zhai, Microporous Mesoporous Mater. 53 (2001) 97–108.
[35] R. Vomscheid, M. Briend, M.J. Peltre, P.P. Man, D. Barthomeuf, J. Phys. Chem. 98 (1994) 9614–9618.
[36] S. Ashtekar, S.V.V. Chilukuri, D.K. Chakrabarty, J. Phys. Chem. 98 (1994) 4878–4883.
[37] G. Sastre, D.W. Lewis, C.R.A. Catlow, J. Phys. Chem. B 101 (1997) 5249–5262.
[38] B.M. Abu-Zied, W. Schwieger, A. Unger, Appl. Catal. B 84 (2008) 277–288.
[39] R.B. Borade, A. Clearfield, J. Mol. Catal. 88 (1994) 249–266.
[40] A.K. Singh, R. Yadav, A. Sakthivel, Microporous Mesoporous Mater. 181 (2013) 166–174.
[41] J.R. Li, R.J. Kuppler, H.C. Zhou, Chem. Soc. Rev. 38 (2009) 1477–1504.
[42] B.M. Lok, C.A. Messina, R.L. Patton, R.T. Gajek, T.R. Cannan, J. Am. Chem. Soc. 106 (1984) 6092–6093.
[43] M. Zamadics, X.H. Chen, L. Kevan, J. Phys. Chem. 96 (1992) 2652–2657.
[44] M. Zamadics, X.H. Chen, L. Kevan, J. Phys. Chem. 96 (1992) 5488–5491.
[45] C. Wang, J. Wang, J. Wang, Appl. Catal. B 204 (2012) 137–147.
[46] J. Wang, T. Yu, X. Wang, G. Qi, J. Xue, Appl. Catal. B 127 (2017) 239–249.
[47] F.D. Renzo, Catal. Today 41 (1998) 37–40.
[48] C.S. Cundy, M.S. Henty, R.J. Plaisted, Zeolite 15 (1995) 353–372.
[49] C.S. Cundy, M.S. Henty, R.J. Plaisted Zeolite 15 (1995) 400–407.
[50] N. Nishiyama, M. Kawaguchi, Y. Hirota, D. Van Vu, Y. Egashira, K. Ueyama, Appl. Catal. A Gen. 362 (2009) 193–199.
[51] Y. Iwase, K. Motokura, T.R. Koyama, A. Miyaji, T. Baba, Phys. Chem. Chem. Phys. 11 (2009) 9268–9277.
[52] Ø.B. Vistad, D.E. Akporiaye, F. Taulelle, K.P. Lillerud, Chem. Mater. 15 (2003) 1650–1654.
[53] G. Liu, P. Tian, Y. Zhang, J. Li, L. Xu, S. Meng, Z. Liu, Microporous Mesoporous Mater. 114 (2008) 416–423.
[54] S.A. Schunk, D.G. Demuth, B. Schulz-Dobrick, K.K. Unger, F. Schüth, Microporous Mesoporous Mater. 6 (1996) 273–285.
[55] A.K. Sinha, S. Seelan, Appl. Catal. A 270 (2004) 245–252.
[56] T. Yu, D. Fan, T. Hao, J. Wang, J. Chem. Eng. 243 (2014) 159–168.
[57] T. Álvaro-Muñoz, C. Márquez-Álvarez, E. Sastre, Catal. Today 179 (2012) 27–34.